A review on the processing accuracy of two-photon polymerization

Xiaoqin Zhou, Yihong Hou, and Jieqiong Lin'

Citation: AIP Advances **5**, 030701 (2015); doi: 10.1063/1.4916886
View online: http://dx.doi.org/10.1063/1.4916886
View Table of Contents: http://aip.scitation.org/toc/adv/5/3
Published by the American Institute of Physics

AIP ADVANCES **5**, 030701 (2015)

A review on the processing accuracy of two-photon polymerization

Xiaoqin Zhou,[1] Yihong Hou,[1] and Jieqiong Lin[2,a]
[1]*School of Mechanical Science and Engineering, Jilin University, Changchun, 130022, China*
[2]*School of Electromechanical Engineering, Changchun University of Technology, Changchun, 130012, China*

(Received 19 January 2015; accepted 19 March 2015; published online 31 March 2015)

Two-photon polymerization (TPP) is a powerful and potential technology to fabricate true three-dimensional (3D) micro/nanostructures of various materials with subdiffraction-limit resolution. And it has been applied to microoptics, electronics, communications, biomedicine, microfluidic devices, MEMS and metamaterials. These applications, such as microoptics and photon crystals, put forward rigorous requirements on the processing accuracy of TPP, including the dimensional accuracy, shape accuracy and surface roughness and the processing accuracy influences their performance, even invalidate them. In order to fabricate precise 3D micro/nanostructures, the factors influencing the processing accuracy need to be considered comprehensively and systematically. In this paper, we review the basis of TPP micro/nanofabrication, including mechanism of TPP, experimental set-up for TPP and scaling laws of resolution of TPP. Then, we discuss the factors influencing the processing accuracy. Finally, we summarize the methods reported lately to improve the processing accuracy from improving the resolution and changing spatial arrangement of voxels. © *2015 Author(s). All article content, except where otherwise noted, is licensed under a Creative Commons Attribution 3.0 Unported License.*
[http://dx.doi.org/10.1063/1.4916886]

I. INTRODUCTION

Three dimensional (3D) micro/nanostructures have widespread applications in the field of microoptics, electronics, communications, biomedicine, microfluidic devices, MEMS, metamaterials. And these fields also put forward higher requirements on the miniaturization and integration of 3D micro/nanostructures, which lead to various micro/nanofabrication technologies like Deep UV lithography,[1] electron/ion beam lithography,[2,3] NanoImprint Lithography (NIL),[4] microstereolithography,[5] Ink-jet printing[6] and self assembly.[7] However, these technologies have encountered many problems inhibiting their actual applications, such as the incapability to fabricate complicated 3D micro/nanostructures, restricted resolution and huge cost. Two-photon polymerization (TPP) is a lay-by-lay method and has great advantages in manufacturing arbitrary three dimensional (3D) micro/nanostructures of various materials such as polymers, hybrid materials, organically modified ceramics (Ormocer), and metals with subdiffraction-limit resolution (down to 100 nm).[8–13]

Since the theoretical proposition of two-photon absorption (TPA)[14] and experimental confirmation,[15] TPP has attracted great interests all over the world. Until in 1997, when Maruo et al.[16] fabricated a spiral structure, the diameter of which is about 7 μm, TPP started to be applied to fabricate 3D micro/nanostructures. In 2001, a microbull with feature sizes of 120 nm beyound the diffraction limit (about 390 nm when λ is 780 nm and NA is 1 in Abbe's diffraction limit formular $d = \lambda/(2\mathrm{NA})$) was fabricated.[8] It was a historical moment, after which various applications of TPP sprang up, such as photonic crystals,[9,17,18] microfluidic device,[19–24] biomedical science,[11,25,26] microoptics,[27–30] dielectrics,[31]

[a]Author to whom correspondence should be addressed. Electronic mail: linjieqiong@mail.ccut.edu.cn

 ©Author(s) 2015

metamaterials[32] and so on. However, among these micro/nanostructures, some structures are fastidious about the processing accuracy. For example, a 5%-lattice-constant fluctuation may completely nullify a defect-couple type frequency add-drop filter in photon crystals.[33] In addition, the surface roughness plays a critical role in the optical performance of the optical components, such as microlens, microprism and so on. Hence, the processing accuracy is a fundamental and important problem needed to be settled.

The factors that influence the processing accuracy include geometry errors of the 3D scanning stages and the principle errors of TPP. TPP is known as a lay-by-lay method and every layer is stacked up by the fundamental element-voxels. Small voxels and tight arrangement are conducive to high accuracy. So the accuracy of the photon-polymerized structures relies on the voxels and their spatial arrangement. In direct laser writing (DLW), resolution and feature size are two different concepts easy to be confused. The former refers to the minimal spacing of two adjacent yet separated structures.[34] In TPP fabrication, many scholars used the resolution but actually referred to the feature size. In terms of an isolate voxel, we regard the resolution as the feature size in this paper.

In this paper, we will first review the basis of TPP micro/nanofabrication, including the mechanism of TPP, the experimental set-up for TPP and the resolution of TPP. Then, we will discuss the factors influencing the processing accuracy of TPP. Finally we will summarize the principles and achievements of the methods to improve the processing accuracy from improving the resolution and changing voxels' spatial arrangement.

II. BASIS OF TPP MICRO/NANOFABRICATION

A. Mechanism of TPP

TPP is a photochemical process initiated by the femtosecond laser beam focused tightly into the volume of the photosensitive resins by a high-numerical-aperture (NA) objective. A normal photo-polymerization process is described in equations (1), (2), and (3).[35] It consists of three processes: the initiation process, the propagation process and the termination process. In the initiation process, photoinitiators (PIs) reach to the excited state (PI^*) by absorption of two photons and decompose to radicals (R·). In the propagation process, the radicals combine with monomers (M) to produce monomer radicals ($RM_n\cdot$). In the termination process, two monomer radicals are combined and the photo-polymerization process is terminated.

$$\mathrm{PI} \xrightarrow{\mathrm{h\nu+h\nu}} \mathrm{PI}^* \rightarrow \mathrm{R}\cdot + \mathrm{R}\cdot, \tag{1}$$

$$\mathrm{R}\cdot + \mathrm{M} \rightarrow \mathrm{RM}\cdot \xrightarrow{\mathrm{M}} \mathrm{RMM}\cdot \ \cdots \rightarrow \mathrm{RM_n}\cdot, \tag{2}$$

$$\mathrm{RM_n}\cdot + \mathrm{RM_m}\cdot \rightarrow \mathrm{RM_{n+m}R}. \tag{3}$$

TPA is the fundamental process of TPP and it is one of the multiphoton absorption (MPA) processes. Different from one-photon absorption (1PA/OPA), in TPA process PIs absorb two photons simultaneously when the initiator molecules transit from a lower energy level to a higher energy level. The energy of 2 photons equals to the subtraction of the two energy levels. There are two types of TPA processes including degenerate process and non-degenerate process.[36] In the degenerate process, the initiator absorbs two photons with the same frequency. Whereas, in the non-degenerate process, the initiator absorbs two photons with different frequencies. Generally, the degenerate TPA is used in the TPP process. TPA is a third-order nonlinear optical process. The absorption rate of energy is proportional to the square of light intensity, which can be expressed as follows:[36]

$$\frac{dW}{dt} = \frac{8\pi^2\omega}{n^2c^2} I^2 \,\mathrm{Im}(\chi^{(3)}), \tag{4}$$

where n is the refractive index, ω is the incident light optical frequency, c is the speed of light in vacuum, I is the intensity of the light and $\mathrm{Im}(\chi^{(3)})$ is the imaginary part of the third-order susceptibility. The cross section for TPA is much lower than that for 1PA, so a ultra-short pulse laser with high intensities in order of $\mathrm{TW/cm^2}$ is needed.[37] For more detail information of the mechanism of multiphoton absorption, refer to Malinauskas et al. (2013).[38] In addition, the polymerization begins

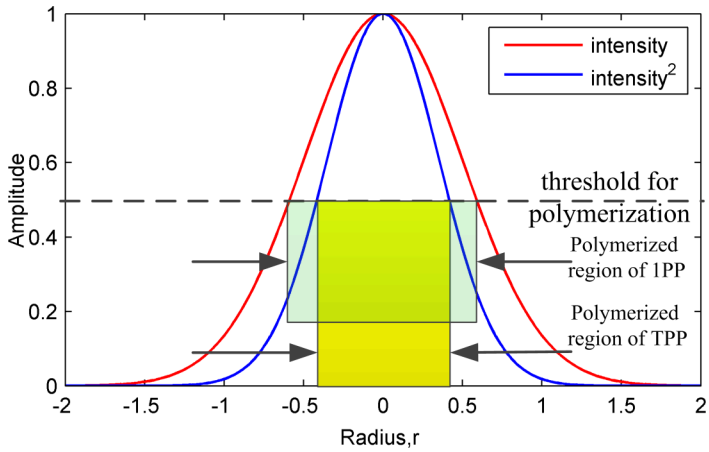

FIG. 1. Distribution of light intensity in the laser focus of a Gaussian beam: $I(r) = I_0\exp(-2r^2/\omega_0{}^2)$, where the beam waist is $\omega_0 = 1$ and the light intensity at the focus is $I_0 = 1$ (dimensionless for clarity). The intensity (red) and the squared intensity (blue) are plotted. Photon- polymerization process takes place at the region where light intensity reaches the threshold for polymerization. So the polymerized region of TPP is smaller than that of one-photon polymerization (1PP).

only when the concentration of radicals exceeds a certain threshold due to radical quenchers in the resin. In other words, there is a threshold of laser intensity when irradiation time equals to a constant or a threshold of irradiation time when laser intensity equals to a constant (see Fig. 1). Both the optical nonlinearity and threshold peculiarity contribute to the resolution beyond the diffraction limit.

B. Experimental set-up for TPP

The optical system for TPP varies according to the different applications. But the basic components are shared in common. The laser beam comes from a mode-locked Ti: sapphire laser and its power is diminished by an attenuator. Then it is expanded by a laser beam expander to reduce the divergence angle and focused tightly into the volume of the resin by a high-numerical-aperture objective (NA of 1.4 and magnification of 100 times for fabricating fine structures). The exposure time is controlled by the shutter. The CMOS/CCD camera enables online process monitoring. The 3D scanning of the laser beam relative to the sample is realized originally by a 3D piezoelectric/PZT stage with high resolution,[16] but its travel and scanning speed are limited. Then, many scholars used a two-dimensional galvanometer scanner combined with a one-dimensional piezoelectric/PZT stage to improve the scanning speed.[35,39] With the development of high-precision positioning technology, 3D linear motor-driven stage[40] and 3D motor-driven linear stage combined with two-dimensional galvanometer[41] were used to fabricate microstructures over a large area reaching to millimeters. In Fig. 2, we summarize these schemes according to the difference of the scanning stage.

C. Resolution of TPP

Resolution is an important parameter representing the feature size of the micro/nanostructures fabricated by TPP. It is relevant to the form of the fundamental unit of TPP, the voxels or lines. Usually, there are two different scanning modes in the fabrication process, the pinpoint scanning (or spot-evaluation) mode and the continuing scanning (or line scanning) mode. The resolution of TPP in the two kinds of scanning modes refer to the feature size of voxels and the width of lines, respectively. Many studies have found that the voxel resembles a spinning ellipsoid whose lateral diameter is smaller than the axial length.[42] So the feature sizes of voxels include the lateral (d) and axial (l) dimensions. The ratio of axial feature size to lateral one is called aspect ratio (α), that is $\alpha = l/d$. Many scholars have studied the scaling laws of the resolution of TPP when changing the parameters, such as the power of femtosecond laser, exposure time, NA of the objective, and have made great achievements.

Schemes	Optical systems	Parameters of the stage	Applications
(a) 3D PZT stage	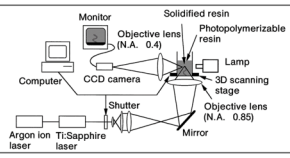	—	Precise micro/nano fabrication
(b) PZT stage and galvanometer	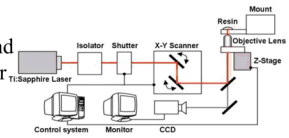	—	Fast precise micro/nano fabrication
(c) 3D linear stage	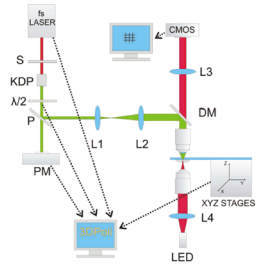	XY-ALS130-150, 150-mm travel Z-ANT-4V, 4-mm travel 300-mm/s scanning speed ~100-nm resolution 200-nm reproducible resolution	Large scale fabrication
(d) 3D linear stage and galvanometer	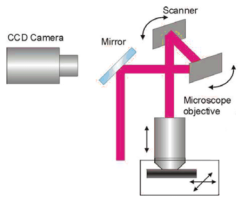	XYZ ABL 10100-LN, 100-mm travel 100-nm.writing accuracy 400-nm positioning accuracy	Fast large scale fabrication

FIG. 2. Different experimental set-up for TPP. (a) 3D PZT stage. Reprinted with permission from S. Maruo et al., Opt Lett **22** (2), 132 (1997). Copyright 1997 The Optical Society. (b) PZT stage and galvanometer. Reprinted with permission from T. W. Lim et al. Microelectronic Engineering **77** (3-4), 382 (2005), Copyright 2005 Elsevier. (c) 3D linear stage. Reprinted with permission from M.-A. Maher et al. **7204**, 72040C (2009). Copyright 2009 The Optical Society. (d) 3D linear stage and galvanometer. Reprinted with permission from S. Passinger et al., in Nanotechnology III, Vol. 6591, pp. 59104. Copyright 2007 Society of Photo Optical Instrumentation Engineers.

In the following, we will analyze the influences of process parameters on the resolution of TPP.

1. Theoretical analysis

The density of radicals, ρ, produced by femtosecond laser pulses can be calculated by solving a simple rate equation (5),[9] and the solution can be expressed as equation (6) assuming the initial density of radicals equals to zero.

$$\frac{\partial \rho}{\partial t} = (\rho_0 - \rho)\sigma_2 I^2, \tag{5}$$

$$\rho = \rho_0(1 - \mathrm{e}^{-\sigma_2 I^2 t}), \tag{6}$$

where,

$$\sigma_2 = \sigma_2{}^{\mathrm{a}}\eta. \tag{7}$$

Here σ_2 is the effective two-photon cross section for the generation of radicals, $\sigma_2{}^{\mathrm{a}}$ the ordinary two-photon absorption cross section, η the efficiency of the initiation process, ρ_0 the primary initiator particle density and I is the photon flux intensity. Suppose the laser beam is a Gaussian beam and the distribution of photon flux intensity $I(r, z)$ at distances of r along the cross section and of z in the propagation direction from the center can be expressed as follows:[43]

$$I(r,z) = I_0\left(\frac{\omega_0^2}{\omega(z)^2}\right)\mathrm{e}^{\frac{-2r^2}{\omega(z)^2}}, \tag{8}$$

where I_0 is the photon flux intensity at the beam center $r = 0, z = 0, \omega_0$ is the beam waist and $\omega(z)$ is the beam radius in the plane with distance of z. In TPP system, a high NA (NA > 1) oil-immersion microscope objective is used and the expression $\omega_0 = \lambda/(\pi \times \mathrm{NA})$ is no longer suitable. A more accurate expression of ω_0 and $\omega(z)$ are expressed as follows:[44]

$$\omega_0 = \frac{\lambda}{\pi \mathrm{NA}}\sqrt{{n_{\mathrm{oil}}}^2 - \mathrm{NA}^2}, \tag{9}$$

$$\omega(z) = \omega_0\sqrt{1 + (\frac{\lambda z}{\pi\omega_0^2})^2}, \tag{10}$$

where λ and n_{oil} denote the wavelength of laser beam and the refractive index of immersion oil, respectively.

The average photon flux intensity at the focus plane I_{focus} is expressed as follows:[45]

$$I_{\mathrm{focus}} = \frac{P}{\pi\omega_0^2\tau f h\nu}, \tag{11}$$

where P, τ, f, h and υ denote the average power, pulse width, repetition frequency, Planck constant and frequency of light, respectively. The frequency of light can be concluded from $\upsilon = \mathrm{c}/\lambda$, where c is the speed of light. The relationship between I_0 and I_{focus} can be expressed as follows:[45]

$$I_0 = \frac{2e^2}{e^2 - 1}I_{\mathrm{focus}} \approx 2.3 I_{\mathrm{focus}}. \tag{12}$$

The photon-polymerization is initiated where the density of radicals $\rho(r,z)$ exceeds the threshold ρ_{th}, that is $\rho(r,z) \geq \rho_{\mathrm{th}}$. The photon flux intensity at the focal plane ($z = 0$) reaches the maximum, where $I(r,z) = I(r,0) = I_0\exp(-2r^2/{\omega_0}^2)$. Neglecting the losses of radicals between the laser pulses, we can obtain the following estimation for the voxel diameter from the above equations.

$$d(P,t) = \omega_0\left(\ln\frac{\sigma_2 {I_0}^2 n\tau}{C}\right)^{1/2}, \tag{13}$$

where $n = ft$ is the number of pulses, t is the total processing-irradiation time and C is defined as the following equation:

$$C = \ln[\rho_0/(\rho_0 - \rho_{th})]. \tag{14}$$

The axial photon flux intensity can be expressed as $I(z) = I_0{\omega_0}^2/\omega(\mathrm{z})^2$. Hence, the length of voxel is depressed as the following equation:

$$l(P,t) = 2z_R\left[\left(\frac{\sigma_2 {I_0}^2 n\tau}{C}\right)^{1/2} - 1\right]^{1/2}, \tag{15}$$

where z_{R} is the Rayleigh length, which is defined as the following equation:

$$z_R = \frac{\pi\omega_0^2}{\lambda}. \tag{16}$$

The numerical analysis of the scaling laws of the diameter and length of the voxels are shown in Fig. 3. The process parameters are listed in TABLE I.

2. Experimental analysis

The theoretical analysis of the resolution of TPP is shown above. However, it is not enough to analyses the actual scaling laws of voxels due to various reasons. Here, we summarize the studies of the isolate voxel in chronological order as shown in TABLE II.

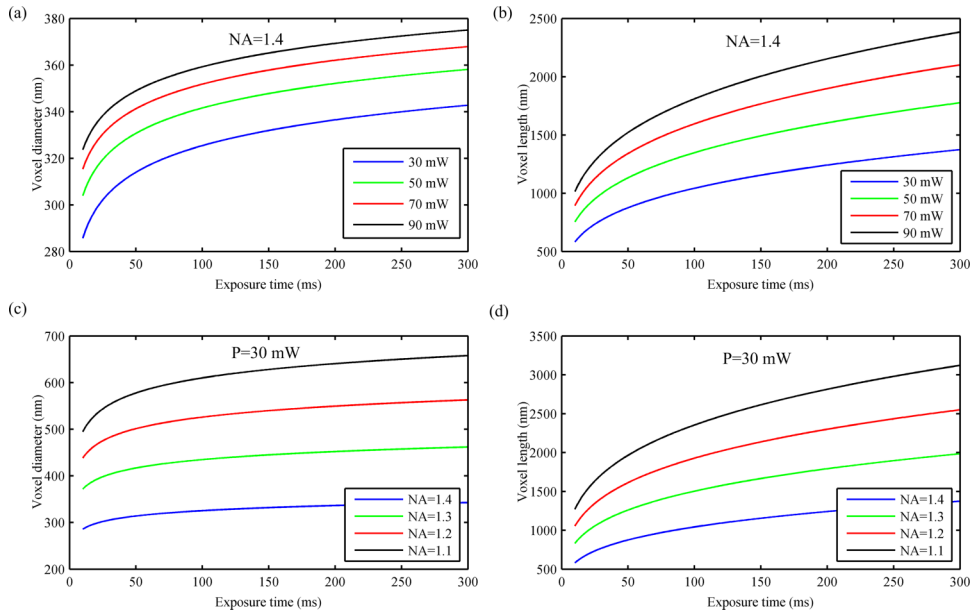

FIG. 3. The numerical analysis of the scaling laws of the diameter and length of the voxels. (a). Scaling laws of the diameter with respect to the exposure time at different power P=30, 50, 70, 90 mW and NA=1.4. (b) Scaling laws of the length with respect to the exposure time at different power P=30, 50, 70, 90 mW and NA=1.4. (c) Scaling laws of the diameter with respect to the exposure time at NA=1.1, 1.2, 1.3, 1.4 and P=30 mW. (d) Scaling laws of the length with respect to the exposure time at NA=1.1, 1.2, 1.3, 1.4 and P=30 mW.

TABLE I. Values of process parameters used for numerical analysis.

Parameter	Value-units
wavelength of laser beam-λ	780 nm
the refractive index of immersion oil-n_{oil}	1.515
pulse width-τ	100 fs
repetition frequency-f	80 MHz
the effective two-photon cross sectin-σ_2	3×10^{-55} cm^4 s
the primary initiator particle density-ρ_0	2.4%[9]
threshold of density of radicals-ρ_{th}.	0.25%[9]
Planck constant-h	6.62606896×10^{-34} J $\cdot$ s
speed of light in vacuum-c	3×10^{8} m/s

The models for initial voxels formation and growth are shown in Fig. 4. Focal spot duplication is related to the square of light intensity. The initial voxels take the focal spot shape defined by the square of light intensity relative to the threshold level. When laser power increases, the voxels expand in all dimensions. Voxel growth is related to the radical diffusion and the voxel grows in the following ways : (i) molecules entangled inside a voxel bulk extend at their active dangling ends by accepting new monomers, wherein the chain reaction proceeds; (ii) the dangling ends meet monomer radicals, either long-chain or short-chain ones, as is a polymerization termination process; and (iii) oligomer and long-chain monomer radicals may be encapsulated and entangled into the surface layers due to the chain elongation in the earlier two processes.[48]

III. FACTORS INFLUENCING THE PROCESSING ACCURACY

The processing accuracy of a 3D micro/nanostructure refers to the dimensional accuracy, shape accuracy and surface roughness. The factors that influence the processing accuracy include geometry errors of the 3D scanning stages and the principle errors of TPP.

TABLE II. Summary of the experimental analysis of the isolate voxels.

References	Topics	Conclusions
H.-B. Sun et al. (2002)[46]	Three-dimensional focal spots	An ascending scan method was utilized to achieve isolated complete 3D voxels. The initiator transformed the quadratic light intensity distribution to a linear radical concentration distribution.
H.-B. Sun et al. (2003)[47]	Experimental investigation of single voxels	Variation of the beam polarization direction relative to the objective led to corresponding orientation rotation of voxels, while their size and shape remain unchanged. A lower NA produced a slimmer voxel. Short exposure time produced a small voxel. simultaneous recording of zeroth- and higher-order diffraction patterns.
H.-B. Sun et al. (2003)[48]	Scaling laws of voxels in the courses of varying laser power and changing exposure duration	Increasing laser power brought about slimmer voxel than increasing exposure time because of the laws of Focal Spot Duplication and Voxel Growth they followed.
DeVoe et al. (2003)[49]	Voxel shapes	The voxel was asymmetric (aspect ratio of 4:1 or greater) at high dose and nearly spherical at low dose (aspect ratio 1:1 or lower) regardless of the type of polymerization systems.

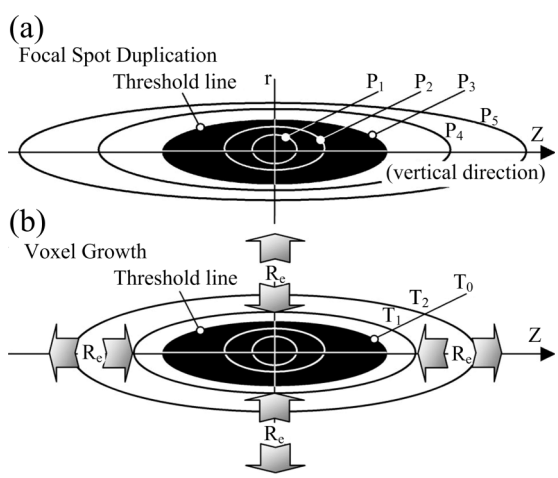

FIG. 4. Models for initial voxels formation and growth. (a) Focal spot duplication and (b) voxel growth. Reprinted with permission from H.-B. Sun et al., Applied Physics Letters **83** (6), 1104 (2003). Copyright 2003 AIP Publishing.

The 3D motion of the laser beam relative to the sample is realized by the 3D piezoelectric/PZT stage or linear motor-driven stage, sometimes combined with a two-dimensional galvanometer. The resolution of a piezoelectric/PZT stage is usually several nanometers and the accuracy of the scanner-based writing is about 100 nm, while the position accuracy over the complete travel range in linear motor-driven stage is better than 400 nm.[50] The geometry errors of these stages can cause the offset of the ideal position and posture of the voxels (Take the x-stage for example. See Fig. 5). Hence, the high-precision stage is needed.

There are inherent principle errors of TPP as a kind of 3D printing technology, such as step effect and errors of mathematical model in STL file format as shown in Fig. 6. In STL model, structures are composed of flat triangles. Therefore, there are errors between the CAD model and STL model. Even though the errors can be reduced by controlling the size of the triangles, which leads to much processing time, the errors cannot be eliminated.

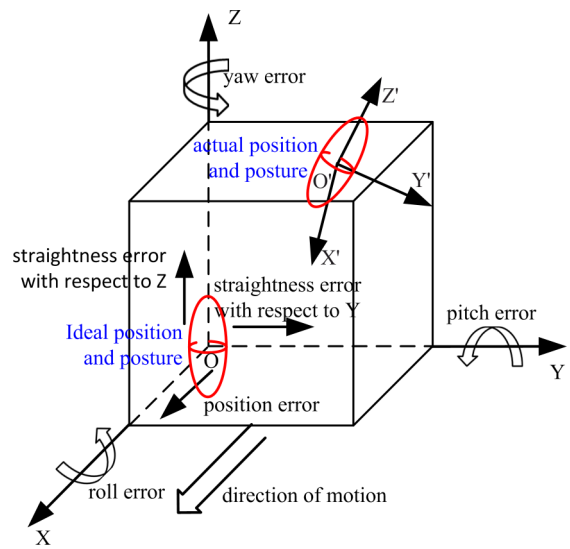

FIG. 5. Geometry errors of x stage cause the offset of the ideal position and posture of the voxels. The six geometry errors of x-stage include three translation errors (position error and two straightness errors) and three rotational errors (roll error, yaw error and pitch error).

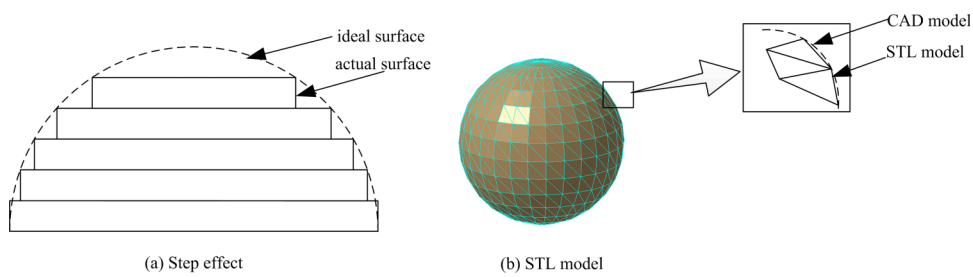

FIG. 6. Principle errors of 3D printing. (a) Step effect and (b) Errors of STL model of a sphere.

The micro/nanostructures are formed by the stack of the voxels, so the resolution and spatial arrangement of the voxels play an important role in fabricating high precise structures. The voxel resembles a spinning ellipsoid, so we use the diameter (d) and length (l) as the features of a isolate voxel. When voxels are arranged in three dimensional space, the overlap δ is an important parameter determining the surface roughness which is defined as follows:[38]

$$\delta = \frac{d - dx}{d} \times \frac{l - dz}{l}, \tag{17}$$

where, dx is the distance of two voxels in x direction and dz is the layer thickness (distance in z direction) (see Fig. 7).

Surface roughness Ra is usually used to evaluate the quality of the surface of the micro/nanostructures and it is defined as follows:

$$Ra = \frac{1}{lr} \int_0^{lr} |Z(x) - Z_0| \, dx \approx \frac{1}{n} \sum_{i=1}^{n} |Z_i| \,, \tag{18}$$

where, lr is the scanning length, $Z(x)$ is the height at each point, Z_0 is the average height, n is the sampling number and Z_i is the height at ith sampling point.

The relationships between the surface roughness and the resolution of TPP and the overlap of voxels are shown in Fig. 8. So, small voxels and big overlap are helpful to acquire precise micro/nanostructures.

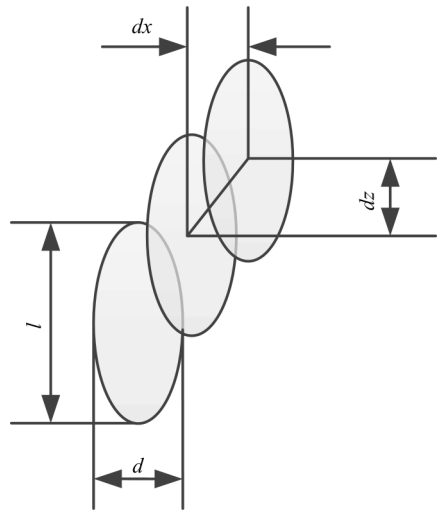

FIG. 7. Illustration of overlap of voxels. It is a function of distances of two voxels in x and z direction.

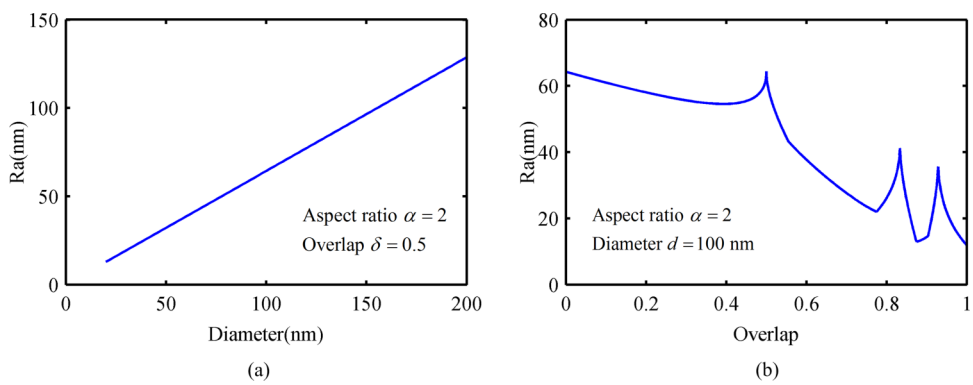

FIG. 8. Numerical analysis of the relationship between the roughness and the diameter and the overlap of the voxels. (a) With decreasing of the diameter, the roughness *Ra* is diminishing at the condition of $\alpha = 2$, $\delta = 0.5$. (b) The roughness *Ra* fluctuates and tends to decrease as the aspect ratio α increasing at the condition of $\alpha = 2$, $d = 100$ nm.

In addition to the above factors influencing the processing accuracy, shrink and deformation due to low mechanical strength during the developing process cannot be ignored when fabricate precise micro/nanostructures. Sometimes, shape distortion happens in near flat region when the layer is too thick.

IV. METHODS TO IMPROVE THE PROCESSING ACCURACY

In this section, various methods to improve the processing accuracy are summarized according to their principles (see TABLE III) and detailed information about them is introduced in the following.

A. Improving the resolution of TPP

1. Changing the process parameters

Process parameters include laser power, exposure time and NA of the objective. In terms of controlling the exposure time, there are two kinds of methods, controlling the shutter and changing the scanning speed, which are used in pinpoint scanning mode (PSM) and continuing scanning mode (CSM), respectively. PSM has a longer exposure time due to the lower mechanical response of the shutter, whereas CSM can be used easily to achieve a higher resolution by changing the scanning speed. The achievements are summarized in TABLE IV at different experimental conditions.

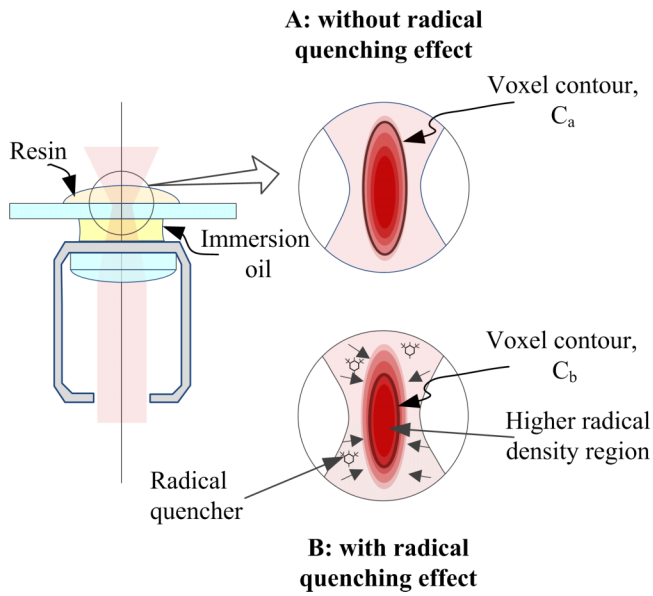

FIG. 9. Schematic illustration of radical quenching mechanism. In case the radical quencher is mixed into the original resin, the voxel size (C_b) is reduced comparing to the case of the original resin only used (C_a). Reprinted with permission from S. H. Park et al., Macromol Res **14** (5), 559 (2006). Copyright 2006 Springer.

TABLE III. Summary of different methods to improve the processing accuracy.

Factors influencing the processing accuracy	Methods	References
resolution of TPP	Changing process parameters	S. Kawata et al. (2001)
		D. Tan et al. (2007)
		Dong et al. (2008)
	Radical Quencher	K. Takada et al. (2005)
		S. H. Park et al. (2006)
	Photoinitiators	J.-F. Xing et al. (2007)
	STED-like lithography	L. Li et al. (2009)
		J. Fischer et al. (2010)
		Y. Cao et al. (2011)
		R. Wollhofen et al. (2013)
shrink	Shape precompensation	H.-B. Sun et al. (2004)
deformation	Multipath scanning method	D.-Y. Yang et al. (2007)
shape distortion	Two-dimensional slicing method	C.-Y. Liao et al. (2007)
step effect	Increasing the voxel's overlap	K. Takada et al. (2005)
	Subregional slicing method	S. H. Park et al. (2005)
	Annular scanning mode	R. Guo et al. (2006)
	Equal-arc scanning	D. Wu et al. (2010)

TABLE IV. The efforts to improve the resolution of TPP by changing the process the parameters.

	Conditions		
References	Laser power	Exposure time/scan speed	Achievements
S. Kawata et al.[8]	137-PJ pulse energy	-	120-nm spatial resolution
Dong et al.[45]	2.5 mW	1.07 ms	50-nm linewidth
D. Tan et al.[51]	35 mW	600 μm/s	23-nm linewidth

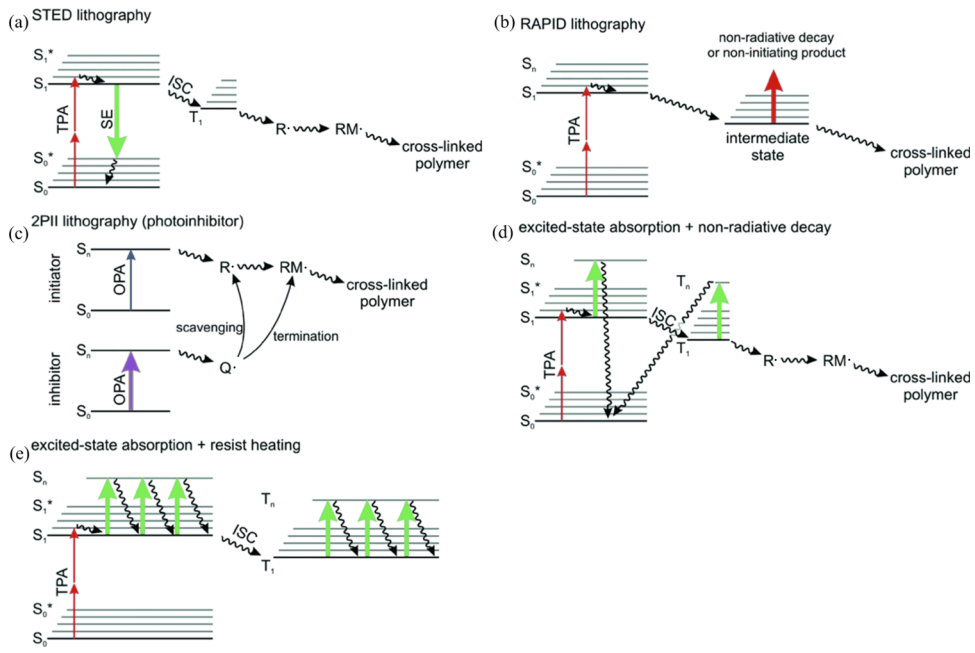

FIG. 10. Schematic diagrams of the depletion mechanisms in STED-like lithography. (a) STED lithography. (b) RAPID lithography. (c) Two-color photo-initiation/inhibition (2PII) lithography. (d) Excited-state absorption. (e) Resist heating. Reprinted with permission from J. Fischer et al., Laser & Photonics Reviews **7** (1), 22 (2013). Copyright 2012 John Wiley and Sons.

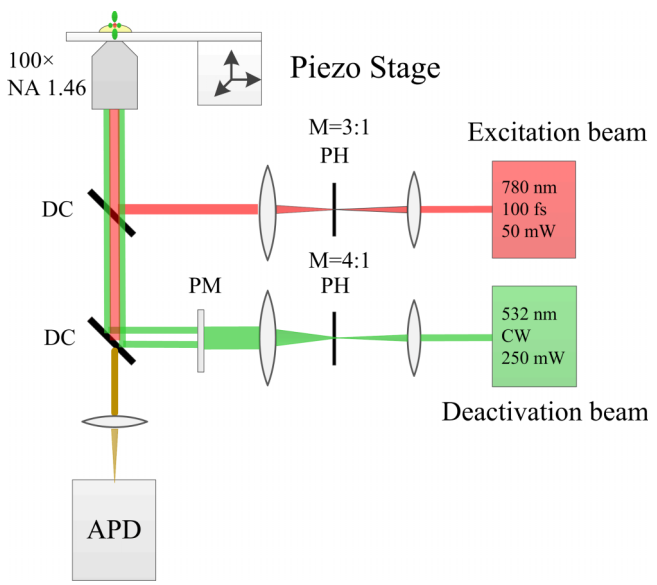

FIG. 11. Setup for STED lithography. Two photon excitation at 780 nm and depletion at 532 nm. PH: pinholes for mode purification, PM: 2π spiral phase plate to create donut beam, objective: 100x NA = 1.46, APD: avalanche photodiode, DC: two dichroic mirrors.

2. Radical Quencher

The mechanism of TPP is shown in section II. Different from normal photo-polymerization process, the quenching process is expressed in equations (1), (19), and (20).[52] The radicals (R·) combine with radical quenchers (Q) instead of monomers (M) to produce quenched radicals (RQ·) and then RQ· are deactivated by irradiation or release of heat. So the radical quenchers prevent the reactions

TABLE V. Summary of recent achievements to improve the resolution of TPP using STED-like lithography.

		experimental conditions						feature size[e]	
		excitation beam		deactivation beam (nm)					
References	methods	λ[a] (nm)	P[b]	λ[a] (nm)	P[b]	t[c] (ms)	v[d] ($\mu m/s$)	lateral (nm)	axial (nm)
L. Li et al. (2009)[58]	RAPID	800 (200 fs)	10 mw	800 (CW)	93 mw	-	-	-	40 (V)
J. Fischer et al. (2010)[59]	ITX-based depletion lithography	810 (150 fs)	13.5 mw	532 (CW)	70 mw	-	100	65 (L)	-
Y. Cao et al. (2011)[60]	2PII	480 CW	200 nw	375 (CW)	6 μw	0.4 s	-	40 (V)	-
			200 nw		2 μw	-	3	130 (L)	-
R. Wollhofen et al. (2013)[34]	STED	780 (110 fs)	3.2 mw	532 (CW)	5.8 mw	-	90	54 (L)	-

[a]Wavelength of laser beam. Pulse width (fs) is included in pulsed laser and CW stands for continuous laser.
[b]Power of laser beam.
[c]Exposure time.
[d]Scanning speed.
[e]The feature sizes include the lateral and axial dimensions in the form of voxels (V) and lines (L).

of photo-polymerization.

$$R\cdot + Q \rightarrow RQ\cdot, \tag{19}$$

$$RQ\cdot \rightarrow RQ + \text{heat or } h\nu. \tag{20}$$

The density of radicals is proportional to the square of the photon flux intensity from equation (6), and the photon flux intensity is the function of radius to the axis of the laser beam and the propagation distance among the axis as expressed in equation (8). So the density of radicals of the inner part of the focus is high enough to diminish the quenching effect and the photo-polymerization at the region far from the focus is inhibited by the quenching effect. As a result, the feature size of voxels is reduced. The schematic illustration of radical quenching mechanism is shown in Fig. 9. It is apparent that the voxel using radical quenchers is smaller than the one that doesn't using radical quenchers. Therefore, we can use the radical quenchers to improve the resolution of TPP.

In 2005, K. Takada et al. improved the lateral spatial resolution of the polymerized lines from 120 nm to around 100 nm when the concentrations of the additional initiator and quencher are 0% and 0.8 wt. %, respectively.[53] In 2006, S. H. Park et al. studied the quenching effect at different concentration of radical quencher and improved the lateral resolution of the line patterns almost to 100 nm by using 2,6-di-tert-butyl-4-methylphenol (DBMP) as the radical quencher.[52] At the same time, they pointed out that the quenching effect would reduce the mechanical strength of polymerized structures due to their short chain lengths.[52]

3. Design of high efficiency photoinitiators

A highly sensitive and efficient photoinitiator can contribute to low threshold and short exposure time, which would reduce the size of the region where radicals are initially generated and decrease the number and diffusion of radicals, respectively.[54,55] Therefore, it can be helpful to improve the resolution of TPP.

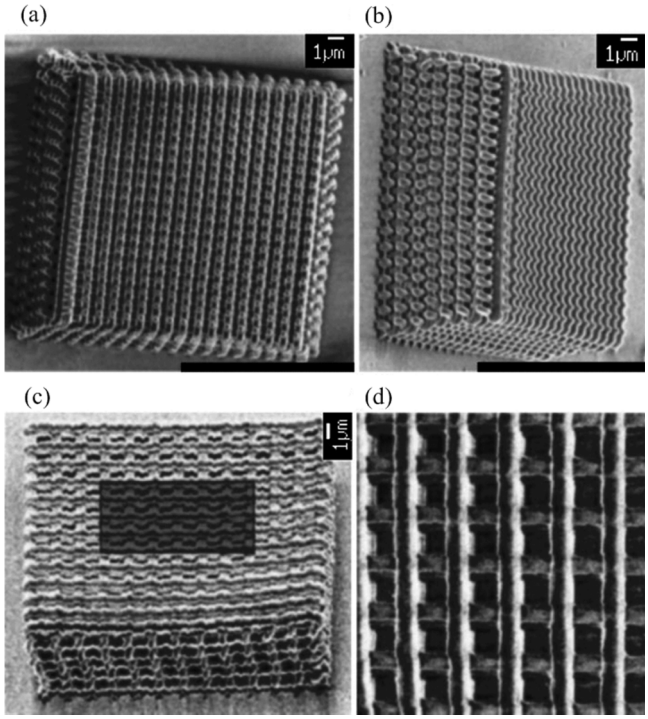

FIG. 12. SEM images of fabricated photonic crystals. All structures were designed with a horizontal cross section of 20 μm×20 μm. (a) No precompensation, top area shrunk to 17 μm×17 μm. (c) A nearly cubic photonic crystals structure after precompensation according to calculated deformation. (b) and (d) are from the same samples as (a) and (b), respectively. Notice the highlight region in (c) was clockwise rotated by 90° and shown in (d). Their shape difference is caused by different view angle. Reprinted with permission from H.-B. Sun et al., Applied Physics Letters **85**(17), 3708 (2004). Copyright 2004 AIP Publishing.

J.-F. Xing et al.[54] fabricated a line with a width of 80 nm by using an anthracene derivative as a highly sensitive and efficient photoinitiator with a laser power of 0.8 mW and a linear scanning speed of 50 μm/s.

4. STED-like lithography

In the past few years, with the development of simulated emission depletion (STED) microscopy technology, it has been used to reduce the feature sizes of TPP. According to the difference of the depletion mechanisms, STED-like lithography include STED lithography, two-color photoimitiation/inhibition (2PII) lithography, Resolution Augmentation through Photo-Induced Deactivation (RAPID) lithography and other lithography based on the alternative mechanisms for photo-inhibited polymerization such as Isopropyl thioxantone (ITX)-based depletion lithography.[56] The depletion mechanisms are shown in Fig. 10. In TPP process, PI molecules are excited via TPA, relax to the S1 state and proceed to the triplet (T1) via intersystem crossing (ISC), generate R·, initiate a propagation polymer chain (RM·) and finally yield an irreversibly cross-linked polymer. Whereas, in STED lithography, PI molecules in the S1 state are brought back to the ground state via stimulated emission (SE) (see Fig. 10(a)). In RAPID lithography, PI molecules are excited via TPA and generate an active species in a long-lived intermediate state. Upon light excitation, the intermediate state is deactivated and does not lead to a cross-linking polymerization (see Fig. 10(b)). In 2PII lithography, PI molecules are excited via OPA and generate radicals that can initiate the polymerization. Photoinhibitor molecules are activated via OPA at a different wavelength. The generated non-initiating radicals (Q·) can scavenge initiating radicals and terminate propagating chains (RM·) (see Fig. 10(c)). In Excited-state absorption, after PI excitation, several intermediate states can absorb the depletion light. From such

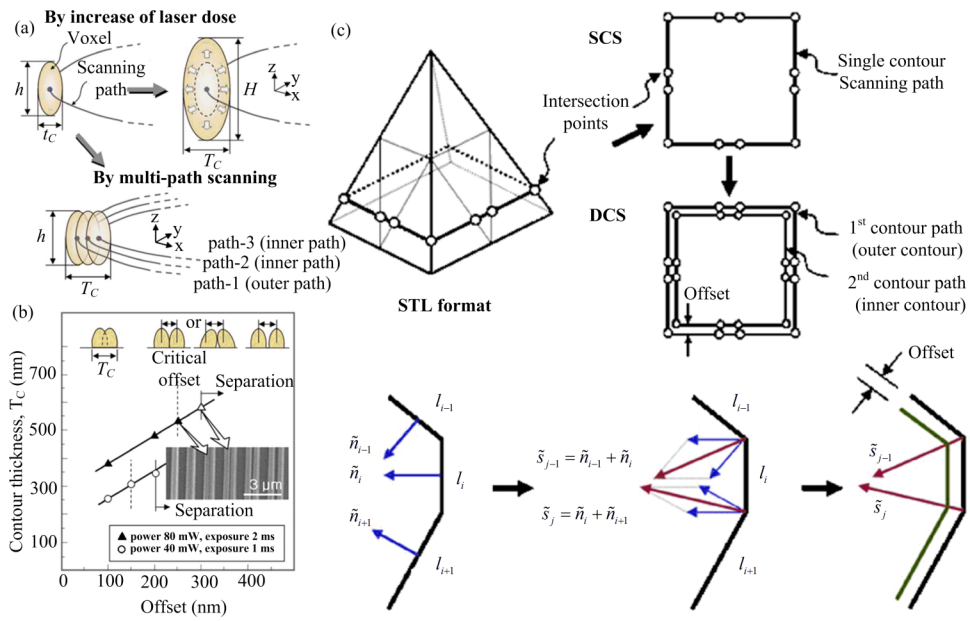

FIG. 13. (a) Schematic illustration of the difference between two approaches to increase contour thickness: by increase of laser dose and by multipath scanning. Comparing to increasing of laser dose, multipath scanning method doesn't change the dimensions of voxel. Hence, it is suit for high precision microfabrication. (b) The variation of the contour thickness with respect to offset for two cases of laser power of 80 mW and exposure time of 2 ms and laser power of 40 mW and exposure time of 1 ms. The inserted SEM image shows the separation between two lines fabricated when the offset is larger than a critical value (in this case, 250 nm). (c) Schematic illustration of the generation procedure of the double-scanning-path using Voronoi's diagram; the second inner contour path is generated using the sum vector, $\tilde{s}$, of two neighboring normal vectors, $\tilde{n}$. Figs. 13(a) and 13(b) are from literature[63] (Reprinted with permission from D.-Y. Yang et al., Applied Physics Letters **90** (7), 079903 (2007). Copyright 2007 AIP Publishing). Fig. 13(c) is from literature[36] (Reprinted with permission from K.-S. Lee et al, Progress in Polymer Science **33** (6), 631 (2008). Copyright 2009 Elsevier Ltd).

highly excited states, nonradiative decay to the ground state can occur (see Fig. 10(d)). In Resist heating, through repeated absorption from an excited-state and nonradiative decay to the same state, the resist can be heated and several resist properties can change with the increased temperature, disturbing the excitation, initiation or polymerization process (see Fig. 10(e)).

The basic idea of these mechanisms is locally prohibiting the formation of an insoluble cross-linked polymer.[56] In these STED-like lithography technologies, two laser beams are used, including the excitation beam and the deactivation beam. The excitation beam initiates the photo-polymerization, whereas the phase shaped deactivation beam inhibits the photo-polymerization around the central excited zone in photophysical or photochemical ways.[57] The setup for STED lithography is shown in Fig. 11. The voxel scaling depends on the phase mask. The donut focus reduces the lateral feature size and the bottle-beam focus has a more obvious reduction on the axial feature sizes.[56]

Using STED-like lithography, many exciting results have been achieved. The efforts are summarized in Table V.

B. Improving the dimensional and shape accuracy

1. Shape precompensation

The realization of the photonic band gap of photonic crystals depends on its fine structural parameters. Photonic crystals fabricated by TPP will shrink due to higher mass density in solid phase than in liquid status, which will invalidate the photonic crystals. To solve the problem, a shape precompensation method was proposed.[61] The shrinkage rate is a material-dependent constant and can be measured experimentally, so the dimension of photonic crystals at different height can add a shrink rate in the design stage. The demonstration of the shape precompensation method is shown in Fig. 12.

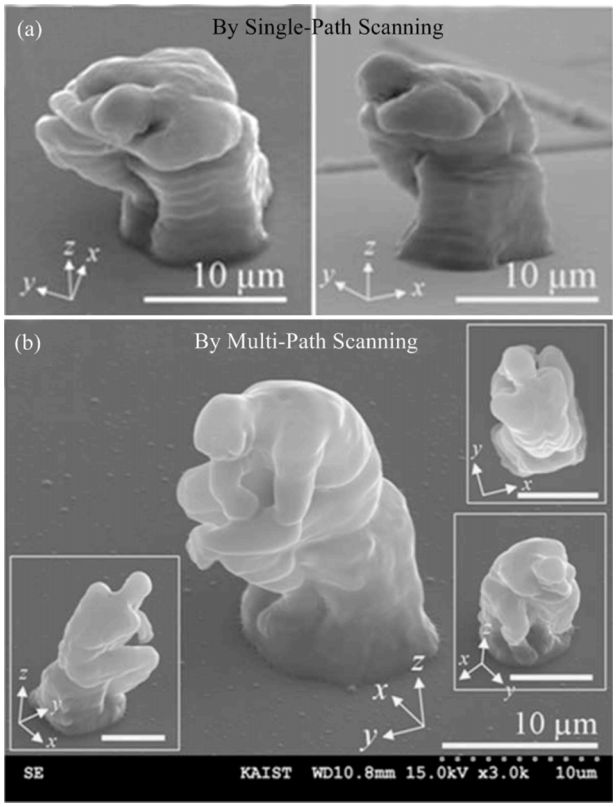

FIG. 14. SEM images of "micro-Thinker" fabricated using two different scanning methods. (a) The "micro-Thinker" fabricated using single-path scanning method failed due to the flow and surface tension of a developing material. (b) The "micro-Thinker" fabricated using multi-path scanning method is reproduced. The insets are the same micro-Thinker with various view angles, and the scale bars are 10 μm. Reprinted with permission from D.-Y. Yang et al., Applied Physics Letters **90** (7), 079903 (2007). Copyright 2007 AIP Publishing.

2. Multipath scanning method

There are two kinds of scanning modes in TPP micro/nano-fabrication: raster scanning mode and profile/contour scanning mode.[62] In raster scanning mode, the laser focus traces every point that constructing the microstructures. Whereas, in profile scanning mode, the laser focus selectively traces the contour profile of the microstructures. Therefore, the profile scanning is usually used to improve the fabrication efficiency. The shell thickness of the structures fabricated in profile scanning is very thin, so it's easy to deform during the developing process. In order to improve the mechanical strength, two methods are proposed.[63] One is increasing the laser dose and the other one is multi-path scanning (MPS). The differences between them are shown in Fig. 13(a). Both of the contour thickness (t_C) and height (h) are becoming larger by increasing the laser dose. In MPS, only the contour thickness increased. The variation of the contour thickness with respect to the offset of two voxels is shown in Fig. 13(b). Hence, the MPS is more suitable for high precision microfabrication.

The multipath is obtained strictly from two-dimensional sliced data by using a Voronoi diagram.[64] After constructing the dividing lines in an outer contour, offsetting is carried out to generate a new interior contour by connecting intersection points on the dividing vectors.[63] The principle of double-scanning-path is shown in Fig. 13(c). The "micro-Thinker" fabricated using single-path scanning (SPS) method and MPS method were compared in Fig. 14. The one fabricated using SPS collapsed as shown in Fig. 14(a). However, the one fabricated using MPS was intact, as shown in Fig. 14(b).

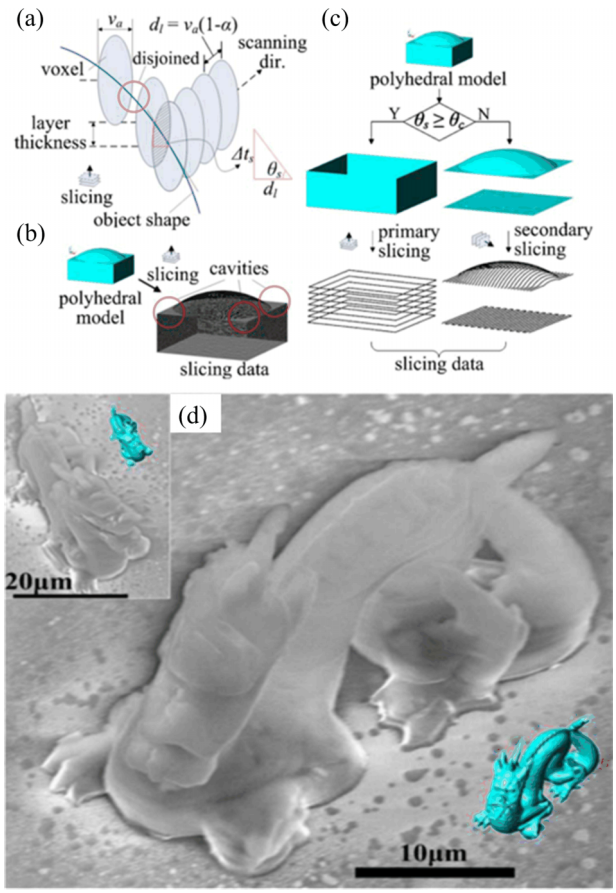

FIG. 15. (a) Schematic diagram of suitable layer thickness (Δt_s) to avoid separation of layers in SSM. (b) Slicing data of the block with a nearly planar area produced by using SSM. It clearly shows cavities occurring in horizontal regions and too small layer thicknesses used. (c) Process flow of the TSM. The slicing data of example in (b) are composed of two slicing data. (d) a microdragon fabricated by TSM. Reprinted with permission from C.-Y. Liao et al., Applied Physics Letters **91** (3), 033108 (2007). Copyright 2007 AIP Publishing.

3. Two-dimensional slicing method

Two-dimensional slicing method (TSM) is used to manufacture the microstructures that have near flat regions.[65] For these structures, fabrication using single-dimensional slicing method (SSM) would need ultrathin layers and long processing time, even cause some defects.

The layer thickness Δt_s is the product of $\tan\theta_s$ and d_l (see Fig. 15(a)), where θ_s is the shape angle and d_l is the lateral voxel distance defined by the following equation:[65]

$$d_l = v_a(1 - \alpha), \tag{21}$$

where v_a is the lateral size of a voxel and α is the overlapping ratio of voxels. At the flat regions, θ_s becomes smaller and the thickness must decrease according to the change of θ_s in order to avoid the layer separation. If the surface of the microstructures is parallel to slicing plane, its contours will be obtained by the slicing method but the area located inside will remain unprocessed and produce cavities, as shown in Fig. 15(b).[65]

The process flow of the TSM is shown in Fig. 15(c). It consists of two slicing phase. In the the primary slicing phase, where the shape angles are greater than the critical slicing angle θ_c specified by the users according to the shape of the microstructure, the thickness is $v_a(1 - \alpha)\tan\theta_c$. In the secondary slicing phase, the thickness is $v_a(1 - \alpha)$ and the slice direction is perpendicular to the previous slicing planes. A microdragon fabricated by TSM (see Fig. 15(d)) showed the effectivity of TSM.

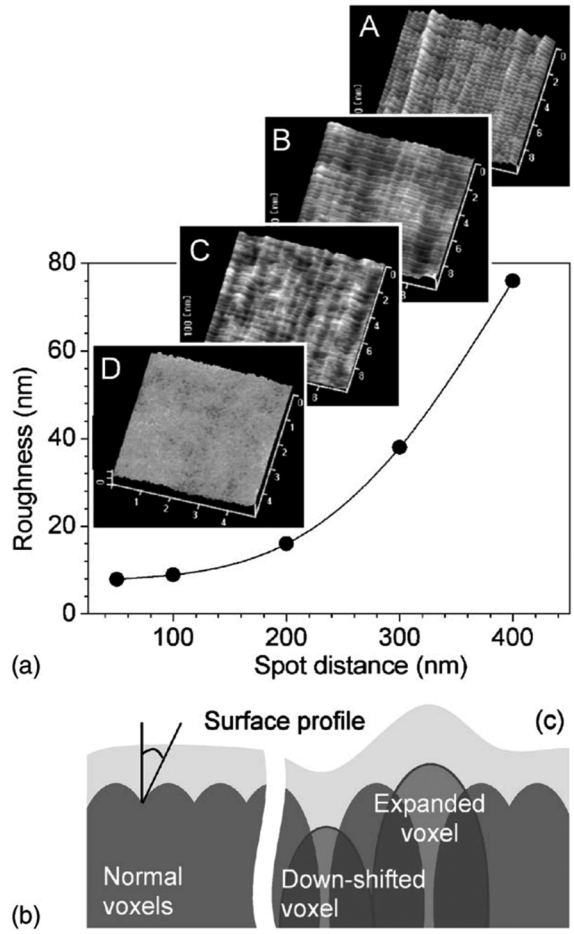

FIG. 16. Mechanism of roughness formation. (a) R–D plot. The insets are AFM images of tube surface with (A) D=300 nm, (B) 100 nm, (C) 50 nm, and (D) a spin-coated polymer surface. (b) Illustrative model to show the voxel-induced roughness cannot propagate to the sample surface when $D < D_s$; (c) therefore ambient and material factors should be responsible for the surface unflatness. Reprinted with permission from K. Takada et al., Applied Physics Letters **86** (7), 071122 (2005). Copyright 2005 AIP Publishing.

C. Improving the surface roughness

1. Increasing the voxel's overlap

The relationship between the spot distance or voxel's overlap and the surface roughness was studied by K. Takada et al.[53] They found that the surface roughness decreased and tended to a constant with the scanning distance decreasing as shown in Fig. 16(a). Because the liquid resins in the concaves boarded by voxel enicult to remove due to the surface Gibbs free energy that is minimized by the negative curvature, the roughness caused by the scan distance is hard to propagated to the surface and negligible compared with those caused by other factors (such as the ambient factors, the jittering of the laser output etc.) when the overlap is high enough.[53] The effect was called self-smoothing effect in D. Wu et al. (2010)[30] as shown in Fig. 16(b). The ambient factors, e.g., vibration may cause voxel displacement and jittering of the laser output would induce the voxel size fluctuation, as shown in Fig. 16(c).

2. Subregional slicing method

The roughness of the lateral surface perpendicular to the stacking direction of the layers depends on the layer thickness. To fabricate high precision 3D micro/nanostructures, smaller layer thickness

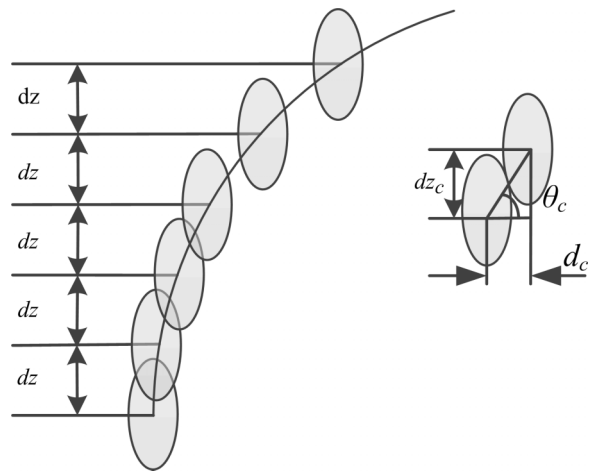

FIG. 17. Illustration of the fabrication with same layer thickness dz. When dz is larger than the critical thickness dz_c, defined as $dz_c = dc\tan\theta c$, the voxels are separated. dc and θ_c represent the critical horizontal distance and the critical slope, respectively.

is required. If all layers are in same thickness regardless of the slope of the structures, this can lead to large processing time. Sometimes, even cause separations of voxels, as shown in Fig. 17. At the same time, the roughness of the regions with steep slopes will be improved slightly. To solve the contradictory between the processing accuracy and processing efficiency, a subregional slicing method (SSM) was developed.[66] The principle of SSM is dividing the 3D microstructure into several subregions on the basis of the geometric slope, and then each of these subregions is uniformly sliced with a layer thickness determined by the geometric slope characteristics of each subregion.[66] That is, subregions with gentle slopes are sliced with thin layer thicknesses, whereas subregions with steep slopes are sliced with thick layer thicknesses. The authors did an experiment to demonstrate the efficiency of SSM, as shown in Fig. 18. The slope of the microjar along the outline, θ_s, can be obtained using the following vector equation:

$$\theta_s = \frac{\pi}{2} - \theta_i = \frac{\pi}{2} - \cos^{-1}\frac{\tilde{N}_i \cdot \tilde{P}_i}{|\tilde{N}_i|\,|\tilde{P}_i|}, \tag{22}$$

where θ_i is the angle between the normal vector of the outlines, $\tilde{N}_i(\tilde{n}_x\,\tilde{n}_y\,\tilde{n}_z)$, and the projected vector of normal vector onto the slicing planes, $\tilde{P}_i$, as depicted in Fig. 18(a). Then the microjar was divided into six regions, region 1 (0°-9.75°), region 2 (9.76°-20.52°), region 3 (20.53°-27.18°), region 4 (27.19°-34.67°), region 5 (34.68°-49.20°), region 6 (49.21°-90°) according to the critical slopes achieved experimentally through fabricating a hemisphere, as shown in Fig. 18(b) and Fig. 18(c).The microjar fabricated using the same layer thickness (56 layers, t_s = 200 nm) has a rough surface in the gentle ascent region, whereas the one fabricated using the SSM (63 layers, t_s = 100 − 200 nm) has a smoother surface even though it was fabricated in a similar time as shown in Fig. 18(d).

3. Annular scanning mode

The conventional scanning model in TPP microfabrication is the parallel linear scanning and it is suitable for most microstructures. However, spherical symmetry structures, such as microlens, fabricated using the parallel linear scanning model is very rough as shown in Fig. 19(a). In order to reduce the surface roughness, a annular scanning method was adopted.[27] A fixed constant layer space ΔZ would introduce serious bench especially at the top part of the lens during fabrication, as shown in Fig. 19(b). So dynamically change the ΔZ to ensure the bench effect is under control according to the scanning space lx. ΔZ is defined by the formula $Z_i = \left[R^2 - (i \cdot lx)^2\right]^{1/2}$, where i and R denote the height of layer and the radius of the sphere, respectively. The optimization result is shown in Fig. 19(c), where the microlens is smoother.

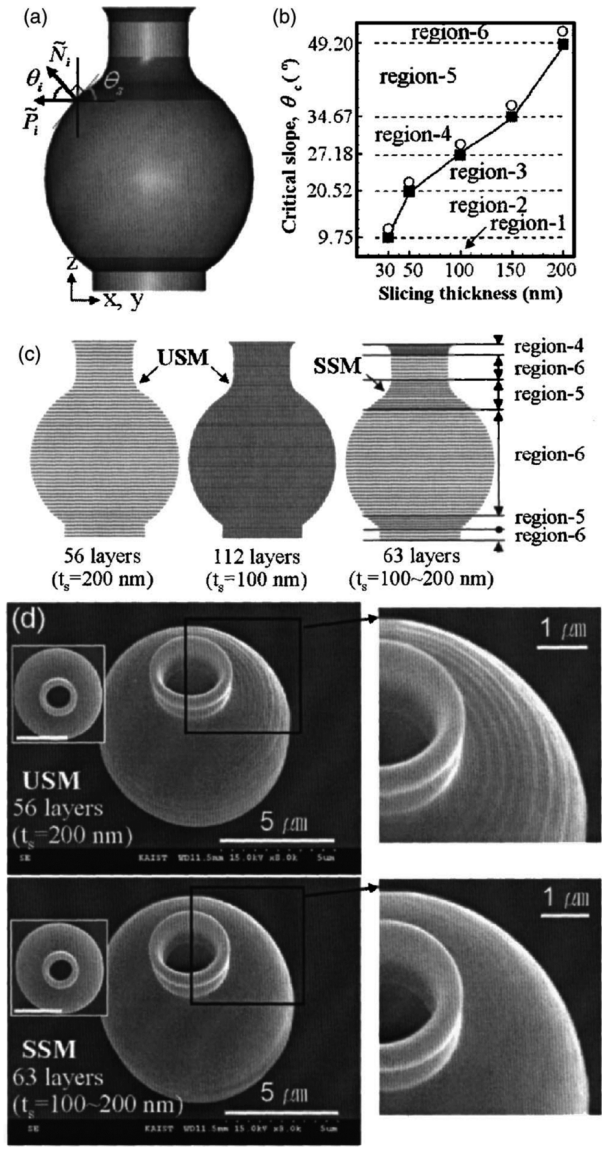

FIG. 18. (a) Designed CAD data and definitions of the normal vector ($\tilde{N}_i$), plane component of the normal vector ($\tilde{P}_i$), and the angle of the slope (θ_s). (b) Variation of the critical slope (θ_c) obtained under the laser power of 60 mW and exposure time of 1 ms (■), and under the laser power of 40 mW and exposure time of 1 ms (○) according to the slicing thickness. (c) Three types of sliced data: 56 layers of uniform thickness 200 nm sliced using the uniform slicing method (USM), 112 layers of uniform thickness 100 nm sliced using the USM; and 63 layers sliced using the SSM. (d) SEM images of microjars fabricated using the USM with 56 layers, and the SSM with 63 layers (inset images: top view of each microjar, scale bar is 5 μm). Reprinted with permission from S. H. Park et al., Applied Physics Letters **87** (15), 154108 (2005). Copyright 2005 AIP Publishing.

4. Equal-arc scanning

In SSM, the layer thicknesses in the same subregion are identical. However, in the equal-arc scanning mode,[30] the layer thickness become a variable expressed as $\Delta h = \Delta L \times \sin\theta$, where ΔL is the arc length and equals to a constant and θ is the sloping angle. Hence, the layer thickness is becoming thinner when θ is becoming smaller. The comparisons between the normal equal-height scanning mode and the equal-arc scanning mode are illustrated in Fig. 20. The microlens fabricated using the equal-arc scanning mode is much smoother than the one using the equal-height scanning mode.

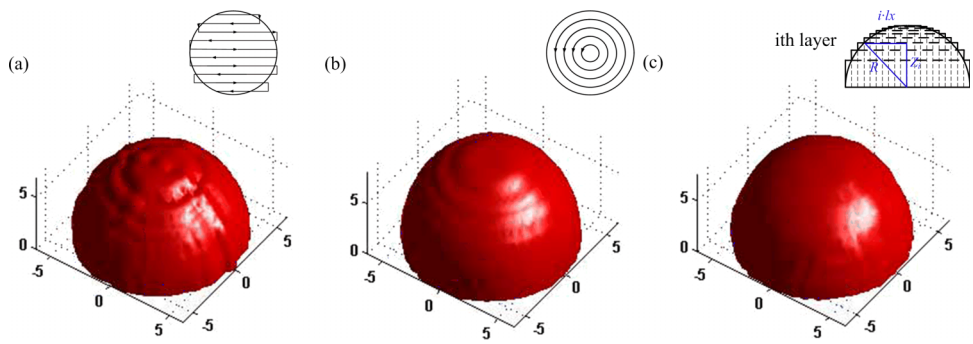

FIG. 19. Simulations of microfabrication scanning method effects on micro lens surface quality: (a) parallel linear scanning method with fixed constant ΔZ, (b) annular scanning method with a fixed constant ΔZ, (c) annular scanning method with a dynamical Z_i. Reprinted with permission from R. Guo, et al., Optics express **14** (2), 810 (2006). Copyright 2006 Optical Society of America.

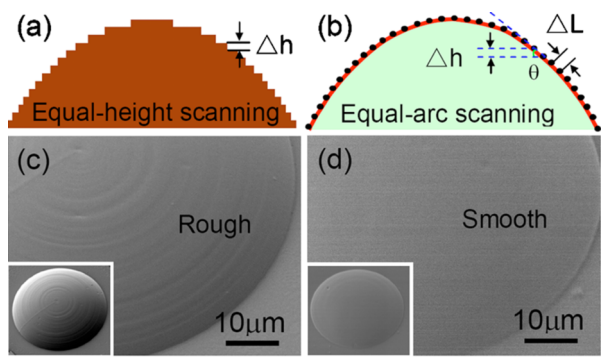

FIG. 20. (a) Equal-height scanning mode. (b) Equal-arc scanning mode. (c) and (d) SEM images of single microlens prepared by the two scanning methods. Reprinted with permission from D. Wu et al., Applied Physics Letters **97** (3), 031109 (2010). Copyright 2010 AIP Publishing.

V. CONCLUSION

TPP as a layer-by-layer technique has great advantages in fabricating arbitrary 3D micro/nanostructures of various materials with ultra-resolution and it has been applied to optics, electronics, communications, biomedicine, microfluidic devices, MEMS and metamaterials. However, accuracy of the micro/nanostructures fabricated by TPP hinders their actual applications especially in optics. In this review, we focus on the improvement of the processing accuracy from improving the resolution of a isolate voxel and changing the spatial arrangement of voxels and introduce efforts to fabricate precise micro/nanostructures. Although great achievements have been made, there is still much work to do. With the demand for large area micro/nanostructures, a long travel stage is needed. As is well known that the accuracy of a long travel stage is worse than the accuracy of a short travel stage. The geometry errors of the stage cannot guarantee exact position and posture of the voxels and bring about the position errors and posture errors of the voxels. The errors existing in voxels will affect the processing accuracy of TPP. Therefore, study of the long travel stage with high precision and compensation of these errors is expected in the future. Besides, errors of the STL file format make it no longer suitable for high precise micro/nanofabrication and a new precise file format is needed urgently. Processing accuracy and efficiency are contradictory. Thin layer thickness means high processing accuracy, but leads to much processing time. The balance between the accuracy and efficiency needs to be considered in the future. We believe that with these issues solved, TPP will have more applications in ultraprecise fields.

ACKNOWLEDGEMENTS

The authors are grateful to the financial support from the National Natural Science Foundation of China (NSFC) (51375060).

[1] W. Bogaerts, V. Wiaux, D. Taillaert, S. Beckx, B. Luyssaert, P. Bienstman, and R. Baets, IEEE journal of selected topics in quantum electronics **8**(4), 928-934 (2002).
[2] C. Vieu, F. Carcenac, A. Pepin, Y. Chen, M. Mejias, A. Lebib, L. Manin-Ferlazzo, L. Couraud, and H. Launois, Applied Surface Science **164**(1), 111-117 (2000).
[3] F. Watt, A. Bettiol, J. Van Kan, E. Teo, and M. Breese, International Journal of Nanoscience **4**(03), 269-286 (2005).
[4] S. Y. Chou, P. R. Krauss, and P. J. Renstrom, Journal of Vacuum Science & Technology B **14**(6), 4129-4133 (1996).
[5] A. Bertsch, S. Jiguet, and P. Renaud, Journal of Micromechanics and Microengineering **14**(2), 197-203 (2004).
[6] M. Walther, A. Ortner, H. Meier, U. Loffelmann, P. J. Smith, and J. G. Korvink, Applied Physics Letters **95**(25), 251107 (2009).
[7] C. Pacholski, A. Kornowski, and H. Weller, Angewandte Chemie **41**(7), 1188-1191 (2002).
[8] S. Kawata, H. B. Sun, T. Tanaka, and K. Takada, Nature **412**(6848), 697-698 (2001).
[9] J. Serbin, A. Egbert, A. Ostendorf, B. Chichkov, R. Houbertz, G. Domann, J. Schulz, C. Cronauer, L. Fröhlich, and M. Popall, Optics letters **28**(5), 301-303 (2003).
[10] A. Doraiswamy, C. Jin, R. J. Narayan, P. Mageswaran, P. Mente, R. Modi, R. Auyeung, D. B. Chrisey, A. Ovsianikov, and B. Chichkov, Acta biomaterialia **2**(3), 267-275 (2006).
[11] A. Ovsianikov, B. Chichkov, P. Mente, N. Monteiro-Riviere, A. Doraiswamy, and R. Narayan, International journal of applied ceramic technology **4**(1), 22-29 (2007).
[12] F. Formanek, N. Takeyasu, T. Tanaka, K. Chiyoda, A. Ishikawa, and S. Kawata, Optics express **14**(2), 800-809 (2006).
[13] V. F. Paz, M. Emons, K. Obata, A. Ovsianikov, S. Peterhänsel, K. Frenner, C. Reinhardt, B. Chichkov, U. Morgner, and W. Osten, Journal of Laser Applications **24**(4), 042004 (2012).
[14] M. Göppert-Mayer, Annalen der Physik **18**(7-8), 466-479 (2009).
[15] W. Kaiser and C. Garrett, Physical Review Letters **7**(6), 229 (1961).
[16] S. Maruo, O. Nakamura, and S. Kawata, Opt Lett **22**(2), 132-134 (1997).
[17] K. Kaneko, H.-B. Sun, X.-M. Duan, and S. Kawata, Applied Physics Letters **83**(11), 2091 (2003).
[18] J. Serbin, A. Ovsianikov, and B. Chichkov, Optics express **12**(21), 5221-5228 (2004).
[19] D. Wu, Q.-D. Chen, L.-G. Niu, J.-N. Wang, J. Wang, R. Wang, H. Xia, and H.-B. Sun, Lab on a chip **9**(16), 2391-2394 (2009).
[20] P. Galajda and P. Ormos, Journal of Optics B: Quantum and Semiclassical Optics **4**(2), S78 (2002).
[21] C. Schizas, V. Melissinaki, A. Gaidukeviciute, C. Reinhardt, C. Ohrt, V. Dedoussis, B. N. Chichkov, C. Fotakis, M. Farsari, and D. Karalekas, The International Journal of Advanced Manufacturing Technology **48**(5-8), 435-441 (2010).
[22] L. Amato, Y. Gu, N. Bellini, S. M. Eaton, G. Cerullo, and R. Osellame, Lab on a chip **12**(6), 1135-1142 (2012).
[23] S. Maruo and H. Inoue, Applied Physics Letters **89**(14), 144101-144101-144103 (2006).
[24] S. Maruo, A. Takaura, and Y. Saito, Optics express **17**(21), 18525-18532 (2009).
[25] A. Ovsianikov, S. Schlie, A. Ngezahayo, A. Haverich, and B. N. Chichkov, Journal of tissue engineering and regenerative medicine **1**(6), 443-449 (2007).
[26] F. Klein, B. Richter, T. Striebel, C. M. Franz, G. v. Freymann, M. Wegener, and M. Bastmeyer, Advanced materials **23**(11), 1341-1345 (2011).
[27] R. Guo, S. Xiao, X. Zhai, J. Li, A. Xia, and W. Huang, Optics express **14**(2), 810-816 (2006).
[28] M. Malinauskas, H. Gilbergs, A. Žukauskas, V. Purlys, D. Paipulas, and R. Gadonas, Journal of optics **12**(3), 035204 (2010).
[29] M. Malinauskas, A. Žukauskas, V. Purlys, K. Belazaras, A. Momot, D. Paipulas, R. Gadonas, A. Piskarskas, H. Gilbergs, A. Gaidukevičiūtė, I. Sakellari, M. Farsari, and S. Juodkazis, Journal of Optics **12**(12), 124010 (2010).
[30] D. Wu, S.-Z. Wu, L.-G. Niu, Q.-D. Chen, R. Wang, J.-F. Song, H.-H. Fang, and H.-B. Sun, Applied Physics Letters **97**(3), 031109 (2010).
[31] T. Kondo, K. Yamasaki, S. Juodkazis, S. Matsuo, V. Mizeikis, and H. Misawa, Thin Solid Films **453-454**, 550-556 (2004).
[32] A. Boltasseva and V. M. Shalaev, Metamaterials **2**(1), 1-17 (2008).
[33] S. Noda, A. Chutinan, and M. Imada, Nature **407**(6804), 608-610 (2000).
[34] R. Wollhofen, J. Katzmann, C. Hrelescu, J. Jacak, and T. A. Klar, Optics express **21**(9), 10831-10840 (2013).
[35] T. W. Lim, S. H. Park, and D.-Y. Yang, Microelectronic Engineering **77**(3-4), 382-388 (2005).
[36] K.-S. Lee, R. H. Kim, D.-Y. Yang, and S. H. Park, Progress in Polymer Science **33**(6), 631-681 (2008).
[37] S. Wu, J. Serbin, and M. Gu, Journal of Photochemistry and Photobiology A: Chemistry **181**(1), 1-11 (2006).
[38] M. Malinauskas, M. Farsari, A. Piskarskas, and S. Juodkazis, Physics Reports **533**(1), 1-31 (2013).
[39] H. B. Sun and S. Kawata, J Lightwave Technol **21**(3), 624-633 (2003).
[40] M.-A. Maher, M. Malinauskas, V. Purlys, M. Rutkauskas, R. Gadonas, J.-C. Chiao, and P. J. Resnick, **7204**, 72040C-72040C-72011 (2009).
[41] S. Passinger, R. Kiyan, A. Ovsianikov, C. Reinhardt, and B. Chichkov, in *Nanotechnology III*, edited by F. Briones (Spie-Int Soc Optical Engineering, Bellingham, 2007), Vol. 6591, pp. 59104–59104.
[42] M. Born and E. Wolf, *Principles of optics: electromagnetic theory of propagation, interference and diffraction of light* (CUP Archive, 1999).
[43] S. Juodkazis, V. Mizeikis, K. K. Seet, M. Miwa, and H. Misawa, Nanotechnology **16**(6), 846-849 (2005).
[44] D. S, L. De, A. J. G. Otuka, V. Tribuzi, and C. R (2012).
[45] X.-Z. Dong, Z.-S. Zhao, and X.-M. Duan, Applied Physics Letters **92**(9), 091113 (2008).
[46] H.-B. Sun, T. Tanaka, and S. Kawata, Applied Physics Letters **80**(20), 3673 (2002).
[47] H.-B. Sun, M. Maeda, K. Takada, J. W. Chon, M. Gu, and S. Kawata, Applied physics letters **83**(5), 819-821 (2003).

[48] H.-B. Sun, K. Takada, M.-S. Kim, K.-S. Lee, and S. Kawata, Applied Physics Letters **83**(6), 1104 (2003).
[49] R. J. DeVoe, H. Kalweit, C. A. Leatherdale, and T. R. Williams, P Soc Photo-Opt Ins **4797**, 310-316 (2003).
[50] A. Ostendorf and B. N. Chichkov, Photon Spectra **40**(10), 72-+ (2006).
[51] D. Tan, Y. Li, F. Qi, H. Yang, Q. Gong, X. Dong, and X. Duan, Applied Physics Letters **90**(7), 071106 (2007).
[52] S. H. Park, T. W. Lim, D. Y. Yang, R. H. Kim, and K. S. Lee, Macromol Res **14**(5), 559-564 (2006).
[53] K. Takada, H.-B. Sun, and S. Kawata, Applied Physics Letters **86**(7), 071122 (2005).
[54] J.-F. Xing, X.-Z. Dong, W.-Q. Chen, X.-M. Duan, N. Takeyasu, T. Tanaka, and S. Kawata, Applied Physics Letters **90**(13), 131106 (2007).
[55] S. M. Kuebler, K. L. Braun, W. Zhou, J. K. Cammack, T. Yu, C. K. Ober, S. R. Marder, and J. W. Perry, Journal of Photochemistry and Photobiology A: Chemistry **158**(2), 163-170 (2003).
[56] J. Fischer and M. Wegener, Laser & Photonics Reviews **7**(1), 22-44 (2013).
[57] A. Spangenberg, N. Hobeika, F. Stehlin, J.-P. Malval, F. Wieder, P. Prabhakaran, P. Baldeck, and O. Soppera (2013).
[58] L. Li, R. R. Gattass, E. Gershgoren, H. Hwang, and J. T. Fourkas, Science **324**(5929), 910-913 (2009).
[59] J. Fischer, G. von Freymann, and M. Wegener, Advanced materials **22**(32), 3578-3582 (2010).
[60] Y. Cao, Z. Gan, B. Jia, R. A. Evans, and M. Gu, Optics express **19**(20), 19486-19494 (2011).
[61] H.-B. Sun, T. Suwa, K. Takada, R. P. Zaccaria, M.-S. Kim, K.-S. Lee, and S. Kawata, Applied Physics Letters **85**(17), 3708 (2004).
[62] T. Tanaka, H.-B. Sun, and S. Kawata, Applied Physics Letters **80**(2), 312 (2002).
[63] D.-Y. Yang, S. H. Park, T. W. Lim, H.-J. Kong, S. W. Yi, H. K. Yang, and K.-S. Lee, Applied Physics Letters **90**(7), 079903 (2007).
[64] D.-S. Kim, Computer-Aided Design **30**(14), 1069-1076 (1998).
[65] C.-Y. Liao, M. Bouriauand, P. L. Baldeck, J.-C. Léon, C. d. Masclet, and T.-T. Chung, Applied Physics Letters **91**(3), 033108 (2007).
[66] S. H. Park, S. H. Lee, D.-Y. Yang, H. J. Kong, and K.-S. Lee, Applied Physics Letters **87**(15), 154108 (2005).